

## Raman intensity and spectra predictions for cylindrical viruses

Eric C. Dykeman, Otto F. Sankey, and Kong-Thon Tsen

*Department of Physics, Arizona State University, Tempe, Arizona 85287-1504, USA*

(Received 3 April 2007; published 11 July 2007)

A theoretical framework for predicting low frequency Raman vibrational spectra of viral capsids is presented and applied to the M13 bacteriophage. The method uses a continuum elastic theory for the vibrational modes and a bond-charge polarizability model of an amorphous material to roughly predict the Raman intensities. Comparison is made to experimental results for the M13 bacteriophage virus.

DOI: [10.1103/PhysRevE.76.011906](https://doi.org/10.1103/PhysRevE.76.011906)

PACS number(s): 87.15.Aa, 87.15.La, 62.30.+d

### I. INTRODUCTION

Viruses are “rigid” spheroidal or cylindrical shells of protein material that contain and protect their genetic material within a core region. Viruses infect bacterium, plant, and animal cells by using the metabolism of the host cell to replicate. Most of the enzymes needed for viral development, growth, and reproduction are created by its infected host cell. In their role as a parasite they may cause severe damage to the host cell. Attempts to intervene and arrest their cycle, for example, by using drugs, must be carefully considered since interfering with these enzymes interferes with the normal processes of the host cell. Viral infestations produce an array of diseases and are a serious health hazard in humans.

A potential benign strategy is to interact directly with the virus’s protein capsid and disrupt its development cycle. One proposal to disrupt the virus is through its low frequency vibrational spectrum. These low frequencies will be sensitive to the size, shape, and protein-protein interactions that adhere the capsid together and hence is virus specific. Ultrasound or inelastic light scattering are potential means to stimulate the vibrational modes of the capsid. If these modes can be excited resonantly, the virus potentially could even be destroyed. Since the resonant frequencies are virus specific, the host cell could conceivably remain undamaged. A successful implementation of this concept has never been achieved, although it is a tantalizing idea with important consequences.

Vibrational modes are also an important diagnostic tool to characterize and analyze nanoscience applications involving viruses. The capsid shell has been used as a scaffolding or template structure in which to build self-assembled machines or devices. One persistent problem in creating nanoparticles is that a synthesis batch has a diversity of sizes. Synthesis and patterning using viral templates is an exciting development that may produce a remedy for this problem. For example, the tobacco mosaic virus has been used to direct the synthesis of semiconductor nanoparticles (CdS and PS) [1] or metals [2]. In another application, the peptide sequence of the virus can be genetically altered to form desirable nucleation sites producing templates that allow tunability of the synthesized structures. The genetics of the M13 virus has been used to control the formation of semiconducting and magnetic nanowires [3]. In all of these applications, the monitoring of the vibrational modes of the viral shell through Raman scattering offers a nondestructive and even noninva-

sive method of following modifications of the viral capsid.

In developing strategies to perform diagnostic applications involving viruses in nanoscience, or to destroy viruses by resonant excitation, a theoretical analysis of viral vibrational frequencies and their measurement by Raman scattering becomes an essential first step. This paper reports on both of these key issues.

The *ab initio* route to study vibrational modes is to atomistically model the virus and diagonalize the force constant matrix (Hessian) along with the mass matrix to obtain the normal modes and eigenfrequencies. The number of atoms that can be treated by this procedure is limited due to computational limitations of creating or diagonalizing large matrices. Since viral capsids generally contain thousands of atoms (or hundreds of thousands or more), the *ab initio* approach is extremely difficult. There has been very recent success at this front, however. Freddolino *et al.*[4] have reported a molecular dynamics simulation of a complete satellite tobacco mosaic virus. This paves the way for such methods, but at the current time such efforts are extraordinary. Another approach is to coarse grain the atomic system with an elastic network model [5,6]. These models have been used to obtain insights into the mechanical properties of viruses.

The low frequency vibrational modes are sensitive to the geometric shape and mass distribution of the capsid and are derived from long wavelength excitations where atomistic details are nonessential. Our model begins by treating the viral capsid as a continuum elastic material that undergoes small elastic deformations. With this assumption, elastic wave theory (EWT) can be used to solve, here analytically, for the vibrational frequencies and displacement patterns of each mode. Such models have a long history, including Lamb’s work on isotropic spheres dating to 1882 [7]. Ford [8] has extended this analysis and has developed analytical models to obtain order of magnitude estimates of the vibrational mode frequencies of viral capsids. In this paper, we apply elastic wave theory to a high symmetry tubular virus which allows an analytical solution of the normal mode frequencies and displacement patterns. For less symmetric geometries, a numerical approach is necessary.

Advancing forward in the same spirit, we develop a companion polarizability model for the Raman intensity. The polarizability model we develop is applicable to continuous isotropic materials, and is derived from an atomistic bond polarizability model [9,10] generalized to the case of a randomized amorphous solid. This polarizability model, the amorphous isotropic bond polarizability (AIBP) model, pre-

dicts Raman intensities, at least qualitatively, and aids in sifting out the origin of the modes observed in experiment. The polarizability model along with the vibrational displacement pattern determined from elastic wave theory completely determines the Raman spectra of our modeled viral capsids. More generally, models of very low frequency vibration and their Raman scattering have generated much interest recently due to advances in nanoparticle synthesis and their uses and characterization [11].

Elastic wave theory and the AIBP model are applied to the M13 bacteriophage and the Raman spectra is predicted. Phage M13 is a relatively simple virus with the shape of a long wormlike cylindrical tube with a length and diameter of roughly 800 and 6 nm, respectively. It has been deeply studied and serves as a model for how complex viruses function. We note, however, that most viruses take on an icosahedral “spherical” shape. We compare our theoretical results for the Raman spectra of M13 with our experimental results which are also reported here in abbreviated form.

The outline of this paper is as follows. In Sec. II we review the EWT for vibrational models of a long (infinite) tube. Section III describes the AIBP model that determines the vibrationally induced polarizability tensor needed to predict the Raman intensity. Further details of the model are described in the Appendixes. Section IV melds together the EWT and AIBP models and derives the expressions for polarization and Raman intensities in the case of a cylindrical viral capsid. Section V applies the theory to M13 bacteriophage and compares with experiment. Finally Sec. VI concludes and summarizes the work.

## II. ELASTIC WAVE THEORY

In EWT of a continuous media, a wave equation governs the displacement  $\vec{\mathbf{u}}$  of the elastic material [12],

$$(\lambda + \mu)\vec{\nabla}(\vec{\nabla} \cdot \mathbf{u}) + \mu\nabla^2\mathbf{u} = \rho\ddot{\mathbf{u}}, \quad (1)$$

where  $\lambda$  and  $\mu$  are the Lamé constants [13],  $\rho$  is the density of the material, and  $\vec{\mathbf{u}}$  is the displacement vector. A complete description can be found in Graff [12]—we give here only the basic elements. The wave equation is simplified by introducing a gauge invariant scalar  $\Phi$  and vector potentials  $\mathbf{H}$  for  $\mathbf{u}$  as

$$\mathbf{u} = \vec{\nabla}\Phi + \vec{\nabla} \times \mathbf{H}. \quad (2)$$

Equation (1) produces the scalar and vector wave equations for longitudinal and transverse waves

$$\nabla^2\Phi = \frac{1}{c_l^2} \frac{\partial^2\Phi}{\partial t^2}, \quad (3)$$

$$\nabla^2\mathbf{H} = \frac{1}{c_t^2} \frac{\partial^2\mathbf{H}}{\partial t^2}. \quad (4)$$

Here  $c_l$  and  $c_t$  are the wave speeds of longitudinal and transverse waves, and are dependent on  $\lambda$ ,  $\mu$ , and the mass density. Specifically, they are given by  $c_l^2 = \frac{(\lambda+2\mu)}{\rho}$  and  $c_t^2 = \frac{\mu}{\rho}$ .

Equations (3) and (4) can then be solved for the case of an infinitely long cylindrical shell with inner radius  $a$  and outer

radius  $b$ . This is the simplest model of an M13 virus [14]. Choosing cylindrical coordinates  $(r, \theta, z)$  with  $z$  along the axis of the tube, the translational invariance produces waves with  $z$  dependence  $e^{ikz}$ . In an infinite periodic system, there is a quasimomentum conservation law for light scattering [15]. The conservation law concerns the wave-vector sum of light and the vibrational mode. Light has a relatively long wavelength ( $\approx 500$  nm) so has a very small wave vector. Thus the wave vector of the vibrational modes that are excited is also very small. This leads to the usual approximation of Raman scattering that the excited modes have  $k \approx 0$ . Finite size effects will alter this conclusion. However, M13 with the relatively long length of about 800 nm is expected to most strongly Raman excite only vibrational modes near  $k=0$ . The oscillating solutions with frequency  $\omega$ , for the general case of any  $k$  vector, are given by

$$\Phi = f(r)\cos(n\theta)e^{-i(kz-\omega t)}, \quad (5)$$

$$H_r = h_r(r)\sin(n\theta)e^{-i(kz-\omega t)}, \quad (6)$$

$$H_\theta = -h_r(r)\cos(n\theta)e^{-i(kz-\omega t)}, \quad (7)$$

$$H_z = h_z(r)\sin(n\theta)e^{-i(kz-\omega t)}, \quad (8)$$

with  $n=0, 1, 2, \dots, \infty$ . The radial functions  $f$ ,  $h_r$ , and  $h_z$  are linear combinations of cylindrical Bessel functions of the first and second kind,

$$f(r) = A_\phi J_n(\alpha r) + B_\phi Y_n(\alpha r), \quad (9)$$

$$h_r(r) = A_r J_{n+1}(\beta r) + B_r Y_{n+1}(\beta r), \quad (10)$$

$$h_z(r) = A_z J_n(\beta r) + B_z Y_n(\beta r). \quad (11)$$

Here,  $\alpha$  and  $\beta$  have been defined as

$$\alpha \equiv \frac{\omega}{c_l}, \quad \beta \equiv \frac{\omega}{c_t}.$$

As noted by Balandin and Fonoberov [14], there exists another solution which corresponds to a multiplication of Eqs. (5)–(8) by a phase factor in  $\theta$ . The additional solutions can be obtained by exchanging  $\cos(n\theta)$  for  $\sin(n\theta)$  and  $\sin(n\theta)$  for  $-\cos(n\theta)$ . As one would expect, either choice of solution will yield the same Raman spectra. We choose to use Eqs. (5)–(8) as the solution to the scalar and vector wave equations. The solutions to the wave equations can then be substituted into Eq. (2) in order to obtain the displacement pattern  $\mathbf{u}$ . Since the additional solutions for the angular dependence result in linearly independent displacement patterns, the Raman intensity must include a degeneracy factor of 2 for  $n > 0$  to incorporate both possible solutions.

The frequencies  $\omega$  and Bessel function coefficients that determine the mode patterns can be found by the application of an appropriate boundary condition. The boundary condition required is that the stress tensor vanish on the inner and outer surfaces of the cylindrical shell, i.e.,  $\sigma_{r\alpha}|_{r=a,b} = 0$  ( $\alpha = r, \theta, \text{ or } z$ ) where  $\sigma_{r\alpha}$  are the radial components of the stress tensor. This yields a  $6 \times 6$  matrix equation in terms of the Bessel function coefficients. A solution is found by varying

$\omega$  until the determinant of the matrix vanishes. This value of  $\omega$  corresponds to a normal mode vibrational frequency of the shell and the corresponding coefficients of the cylindrical Bessel functions  $A_\phi$ ,  $B_\phi$ ,  $A_r$ ,  $B_r$ ,  $A_z$ , and  $B_z$  determine the mode pattern.

To find the zero of the determinant we varied  $\omega$  continuously and calculated the determinant of the  $6 \times 6$  matrix at each step. Once an  $\omega$  was found such that the determinant of the matrix was zero to within a specified tolerance, the  $6 \times 6$  matrix was diagonalized and the eigenvectors corresponding to the zero eigenvalues of the matrix determined the coefficients required to describe the mode pattern. The eigenfrequencies and eigenvectors for M13 are presented in Sec. V.

### III. AMORPHOUS ISOTROPIC BOND POLARIZABILITY (AIBP) MODEL

An oscillating electric dipole produces radiation. In a polarizable medium, an external electric field (laser) induces a

polarization of the medium,  $\vec{P} = \alpha \vec{E}$ . If the polarizability  $\alpha$  of the medium is constant, the induced dipole oscillates at the same frequency  $\omega_L$  as the external field. This produces elastic scattered (Rayleigh scattered) light. However, the polarizability of the medium will vary slightly due to the rearrangement of the nuclei when the medium oscillates (at frequency  $\omega$ ) due to a vibration. The net effect is to produce oscillating dipoles at frequency  $\omega_L + \omega$  and  $\omega_L - \omega$ . This is inelastic Raman scattering by vibrations and the measured frequency shifts (Stokes shift at  $-\omega$  and anti-Stokes shift at  $+\omega$ ) determine the vibrational frequencies.

We model the polarization using a bond-polarization (BP) model where the overall polarization is a sum over contributions coming from each of the bonds of the material. We build on the BP model introduced by Cardona and co-workers [9,10] for semiconductor crystals, but extend it for use with viral capsids treated within continuum elastic theory. By treating the polarizability of peptide bonds as in the BP model, we can accurately reproduce the selection rules for Raman scattering and hopefully obtain a semiquantitative analysis of the relative intensities of permitted vibrational modes. Weaker hydrogen bonding or “van der Waal” bonding is not included within the model. Additionally, the light frequency must not be near resonance with electronic transitions, i.e., the model is nonresonant Raman scattering.

The polarizability of each bond is dependent on the charge density distribution within each bond. The polarization of a bond will be different if the electric field is applied parallel or perpendicular to the bond. The change of polarization of each bond to lowest order in the displacements is linear with the bond distance, and is

$$\alpha(l+dl) = \begin{pmatrix} \alpha_\perp + \alpha'_\perp dl & 0 & 0 \\ 0 & \alpha_\perp + \alpha'_\perp dl & 0 \\ 0 & 0 & \alpha_\parallel + \alpha'_\parallel dl \end{pmatrix},$$

where we have assumed that the bond is orientated along the  $z$  axis. The BP and how it influences Raman scattering is

dependent on two model parameters. The first is  $\alpha'_\parallel$  which describes the change in induced polarization along the axis of the bond due to changes of the bond length, and the second  $\alpha'_\perp$  similarly describes changes perpendicular to the bond. Thus we write the change of the induced polarization due to a small displacement along the bond as

$$\Delta \alpha = \begin{pmatrix} \alpha'_\perp \Delta l & 0 & 0 \\ 0 & \alpha'_\perp \Delta l & 0 \\ 0 & 0 & \alpha'_\parallel \Delta l \end{pmatrix}.$$

This theory has been successfully applied to crystals and molecules [9,10,16,17]. In these applications, the positions of all the atoms are known. Thus usual applications of the BP model are microscopic, taking into account each bond and its orientation. Here we seek an approach that is useful even when we do not know the detailed atomic coordinates, or due to the large number of atoms, we wish to average atomistic details to achieve understanding of the global structure rather than the microscopic structure.

Viral capsids assemble themselves in a symmetric (icosahedral) or periodic (tubular) fashion from a repeated set of proteins. The bonds within the proteins tend to be randomly orientated due to helical or folding properties of the proteins. We view the structure more as a random network or amorphous structure rather than a crystalline one, at least on the length scale of fractions of a light's wavelength. With this framework in mind we average the polarizability tensor for a single bond over all possible orientations. This viewpoint, which we call the amorphous isotropic bond polarizability (AIBP) model is rigorously derived from the bond polarizability model where (i) the bond directions are randomly oriented and (ii) each bond is assumed to be the same.

We now list the major theoretical results of the AIBP model which relate the polarizability derivatives ( $\alpha'_\perp$  and  $\alpha'_\parallel$ ) and the shear and compressional strains to the polarizability per unit volume. The result, derived in Appendix A, is

$$\Delta \alpha = \frac{\alpha_s}{V_b} \mathbf{u}_s + \frac{\alpha_c}{V_b} \text{Tr}(\mathbf{u}) \mathbf{I}, \quad (12)$$

where  $\alpha_s$  and  $\alpha_c$  are parameters that describe the polarizability of the material due to shearing and compressional strains. The strain tensor is given by

$$u_{ij} = \frac{1}{2} \left( \frac{\partial u_i}{\partial x_j} + \frac{\partial u_j}{\partial x_i} \right),$$

and the traceless shear strain tensor is

$$\mathbf{u}_s = \mathbf{u} - \frac{1}{3} \text{Tr}(\mathbf{u}) \mathbf{I}.$$

The parameters  $\alpha_s$  and  $\alpha_c$  and their dependence on  $\alpha'_\perp$  and  $\alpha'_\parallel$  are given in Appendix A. The term  $V_b$  describes the average volume that each bond occupies in the isotropic material. Equation (12) forms the foundation for computing the Raman spectra.

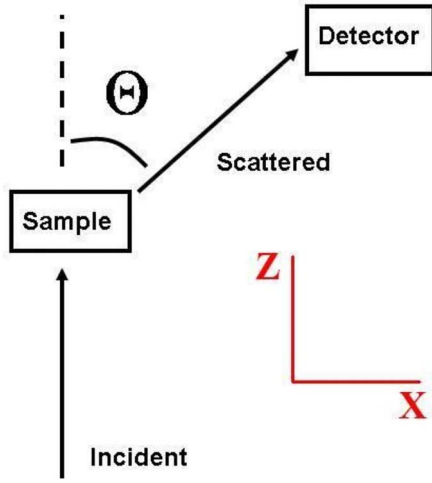


FIG. 1. (Color online) General experimental setup for Raman scattering. Incident light propagates along the  $z$  axis and is then scattered toward the detector located at polar angles  $\Theta$  and  $\Phi$ .  $\Phi$  (not shown) is the standard polar angle in the  $x$ - $y$  plane.

#### IV. RAMAN SPECTRA FOR A CYLINDRICAL CAPSID

In this section, we calculate the relative Raman intensities for a cylindrical viral capsid. To provide a complete theory of the Raman spectra in a continuum approximation, we develop expressions for Raman scattering experiments with the detector at general scattering angles  $\Phi$  and  $\Theta$  as shown in Fig. 1. The expressions are for a randomly oriented sample as in solution. The Raman intensity (the general expressions are derived in Appendix B) for vibrational scattering in a solution can be written in a form similar to the free energy per unit volume of an elastic material,

$$I \propto \frac{1}{2} \frac{\lambda_R}{\omega} [\text{Tr}(\overleftrightarrow{\Delta\chi})]^2 + \frac{\mu_R}{\omega} \text{Tr}(\overleftrightarrow{\Delta\chi})^2, \quad (13)$$

where  $\lambda_R$  and  $\mu_R$  are the Raman intensity coefficients and  $\overleftrightarrow{\Delta\chi}$  is the induced susceptibility. The coefficients  $\lambda_R$  and  $\mu_R$  describe the orientation of the detector (Fig. 1) in the Raman experiment and are given by

$$\lambda_R \equiv [4 - 6 \sin^2\Theta], \quad (14)$$

$$\mu_R \equiv [14 - \sin^2\Theta]. \quad (15)$$

The tensor  $\overleftrightarrow{\Delta\chi}$  is the total induced susceptibility produced by an elastic distortion ( $\mathbf{u}$ ) of the medium. The susceptibility tensor is calculated from the polarizability per unit volume in the AIBP model by integrating Eq. (12) over the volume of the capsid shell

$$\overleftrightarrow{\Delta\chi} = \int \overleftrightarrow{\Delta\alpha} dV.$$

Essentially the displacements  $\mathbf{u}$  given by Eqs. (5)–(8) and Eq. (2) of the EWT along with Eq. (12) of the AIBP model determine the induced susceptibility for a tubular viral capsid. This solution can then be used in Eq. (13) to deter-

mine the relative Raman intensities. The AIBP model is transferable to other systems as well, such as icosahedral capsids, if the appropriate changes to Eqs. (5)–(11) are made.

For the case of a cylindrical tube, it is easier to work with the susceptibility tensor in Cartesian coordinates, so we use the fact that the Cartesian strain is related to the cylindrical strain by a similarity transform,

$$\overleftrightarrow{u}_{cart} = R \overleftrightarrow{u}_{cyl} R^\dagger, \quad (16)$$

where  $R$  is a rotation about the  $z$  axis by the angle  $\theta$  and is given by

$$R = \begin{pmatrix} \cos \theta & -\sin \theta & 0 \\ \sin \theta & \cos \theta & 0 \\ 0 & 0 & 1 \end{pmatrix}.$$

The components of the displacement are given in cylindrical coordinates in the long wavelength approximation ( $k=0$ ) from Eq. (2) and Eqs. (5)–(8) above:

$$u_r(r, \theta, t) = \left( f' + \frac{n}{r} h_z \right) \cos(n\theta) e^{-i\omega t}, \quad (17)$$

$$u_\theta(r, \theta, t) = - \left( \frac{n}{r} f + h'_z \right) \sin(n\theta) e^{-i\omega t}, \quad (18)$$

$$u_z(r, \theta, t) = - \left( \frac{n+1}{r} h_r + h'_r \right) \cos(n\theta) e^{-i\omega t}. \quad (19)$$

Equations (17)–(19) can then be used to yield the components of the strain tensor in cylindrical coordinates:

$$u_{rr} = \left[ f'' + \left( h'_z - \frac{h_z}{r} \right) \frac{n}{r} \right] \cos(n\theta) e^{-i\omega t},$$

$$u_{\theta\theta} = - \left[ \left( h'_z - \frac{h_z}{r} \right) \frac{n}{r} - \left( f' - f \frac{n^2}{r} \right) \frac{1}{r} \right] \cos(n\theta) e^{-i\omega t},$$

$$u_{rz} = - \frac{1}{2} \left[ h''_r + \left( h'_r - \frac{h_r}{r} \right) \frac{n+1}{r} \right] \cos(n\theta) e^{-i\omega t},$$

$$u_{r\theta} = - \left[ \left( f' - \frac{f}{r} \right) \frac{n}{r} + h''_z + \frac{b^2}{2} h_z \right] \sin(n\theta) e^{-i\omega t},$$

$$u_{\theta z} = \frac{1}{2} \left( \frac{n(n+1)}{r^2} h_r + \frac{n}{r} h'_r \right) \sin(n\theta) e^{-i\omega t},$$

$$u_{zz} = 0.$$

Working out the components of the Cartesian strain tensor using Eq. (16), the result is

$$u_{xx} = u_{rr} \cos^2\theta - u_{r\theta} \sin 2\theta + u_{\theta\theta} \sin^2\theta,$$

$$u_{yy} = u_{rr} \cos^2\theta + u_{r\theta} \sin 2\theta + u_{\theta\theta} \sin^2\theta,$$

$$u_{xy} = \frac{1}{2} u_{rr} \sin 2\theta + u_{r\theta} \cos 2\theta - \frac{1}{2} u_{\theta\theta} \sin 2\theta,$$

$$u_{xz} = u_{rz} \cos \theta - u_{\theta z} \sin \theta,$$

$$u_{yz} = u_{rz} \sin \theta + u_{\theta z} \cos \theta,$$

$$u_{zz} = 0.$$

Integrating Eq. (12) over the volume of the shell results in only  $n=0, 1, 2$  terms surviving. Thus the nonzero elements of the induced susceptibility tensor of the shell in each case are

$$\Delta\chi_{xx} = \Delta\chi_{yy} = -\pi \frac{\alpha_s}{V_b} \left( \frac{1}{3} + 2 \frac{\alpha_c}{\alpha_s} \right) \Gamma_0 \quad \text{for } n=0, \quad (20)$$

$$\Delta\chi_{xz} = \Delta\chi_{zx} = -\pi \frac{\alpha_s}{V_b} \Gamma_1 \quad \text{for } n=1, \quad (21)$$

$$\Delta\chi_{xx} = \Delta\chi_{yy} = -\frac{\pi}{2} \frac{\alpha_s}{V_b} \Gamma_2 \quad \text{for } n=2. \quad (22)$$

The quantities  $\Gamma_n$  are integrals of the cylindrical Bessel functions from Eqs. (9)–(11) and they carry information of the normal mode patterns,

$$\Gamma_0 \equiv \int_a^b \alpha^2 r f dr, \quad (23)$$

$$\Gamma_1 \equiv \int_a^b r \left[ \left( \frac{2}{r^2} - \frac{\beta^2}{2} \right) h_r + \frac{h'_r}{r} \right] dr, \quad (24)$$

$$\Gamma_2 \equiv \int_a^b r \left( \frac{3}{r} (f' + h'_z) + \frac{4}{r^2} (f + h_z) - \alpha^2 f - \beta^2 h_z \right) dr. \quad (25)$$

Equations (20)–(22) and (23)–(25) completely determine the susceptibility tensor for a tubular viral capsid. Using these equations and removing common factors, we can write the final relative Raman intensity for the tubular viral capsid as

$$I \propto \frac{(2\lambda_R + \mu_R)}{\omega} \left( \frac{1}{3} + 2 \frac{\alpha_c}{\alpha_s} \right)^2 \Gamma_0^2 \quad \text{for } n=0, \quad (26)$$

$$I \propto 2 \frac{\mu_R}{\omega} \Gamma_1^2 \quad \text{for } n=1, \quad (27)$$

$$I \propto \frac{(2\lambda_R + \mu_R)}{\omega} \frac{\Gamma_2^2}{2} \quad \text{for } n=2, \quad (28)$$

where we have taken into account the degeneracy factor of 2 for the  $n=1, 2$  solutions due to the additional angular solutions as noted above.

To summarize, Eqs. (26)–(28) along with five model parameters (the inner and outer radii, the transverse and longitudinal speeds of sound, and the ratio  $\alpha_c/\alpha_s$ ) are the parameters required to predict the relative Raman intensity for cylindrical viral particles in solution. The present formalism can be extended to other viral geometries, but one must go

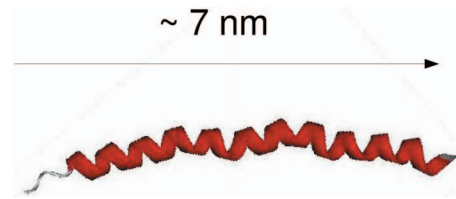


FIG. 2. (Color online) The 50 amino acid peptide building block for the M13 viral capsid.

back to the fundamental equations (12) and (13), with appropriate displacement patterns calculated either analytically or numerically from EWT.

## V. RAMAN SPECTRA OF M13 BACTERIOPHAGE

Using Eqs. (26)–(28) we can now predict the Raman spectra of an M13 bacteriophage. The M13 bacteriophage is a virus with a cylindrical shell formed from a single 50 amino acid peptide building block [18]. This peptide building block is depicted in Fig. 2. The cylindrical viral capsid is assembled by periodically arranging multiple copies around the tube axis. Figure 3 shows a cross section along the  $z$  axis of an M13 bacteriophage. The final capsid structure results in an electrostatically positive region inside the capsid shell, Fig. 3(c), and an electrostatically negative region outside. The genetic material of the virus, a ss-DNA and water, is located along the axis in the center of the shell. Due to the overall negative charge of phosphate in ss-DNA, the electro-

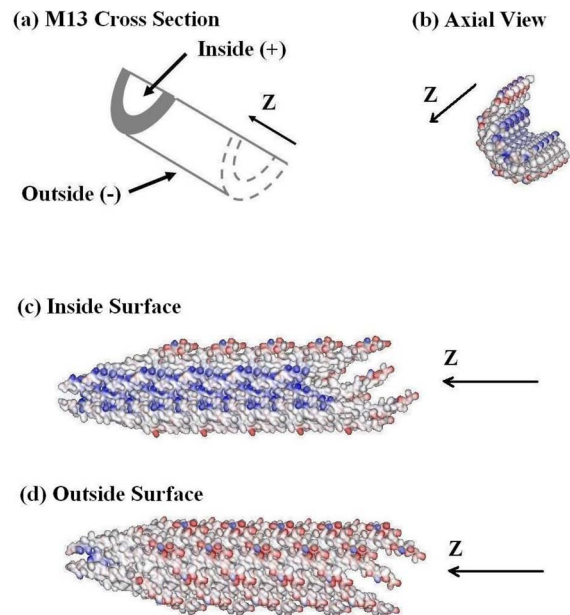


FIG. 3. (Color online) Views of the M13 bacteriophage showing the assembly of the protein building blocks into the completed capsid. Electrostatically negative (red) and positive (blue) regions are shown. (a) Schematic diagram of a cross section of the M13 capsid. (b) Axial view of M13. (c) View of the inside surface of the M13 capsid. One periodic unit of the capsid is shown which is approximately 16 nm in length. (d) View of the outside surface of the M13 capsid.

statically positive inner surface of the capsid provides further stability of the capsid in the presence of ss-DNA. The total axial length of the M13 bacteriophage is roughly 800 nm and the viral capsid has inner and outer radii of roughly 1.9 and 3.4 nm, respectively. These radii were determined by averaging over the cross sectional diameter of the atomistic structure of the viral capsid.

The calculation of the vibrational frequencies and modes requires the longitudinal and transverse speeds of sound. We use values from experiments on lysozyme [19],  $c_t = 915$  m/s and  $c_l = 1817$  m/s. This calculation follows the work of Balandin and Fonoberov [14,20] which was one of the first that used EWT [12,13] with experimentally measured wave speeds to model tubular viruses. Similar approaches have been used by Talati *et al.* who studied “spherical” viruses [21]. The main differences between our calculation and the calculation performed by Balandin and Fonoberov are that (i) we treat the M13 capsid as a cylindrical shell rather than a solid cylinder, and (ii) approximate Raman intensity and corresponding spectral predictions are made using the AIBP model. Figure 4 shows the dispersion relations,  $\omega(k)$ , for  $n=0, 1, 2$  modes of the M13 bacteriophage treating it as a cylindrical shell. Raman scattering is only sensitive to the modes at  $k=0$ . One notes that there are many low frequency modes, say, less than  $15 \text{ cm}^{-1}$ . Thus it is important to go further and offer estimates of their Raman intensity in order to make full contact with experiment.

We have examined the sensitivity of the vibrational frequencies to changes in the inner and outer radii of the tube. To do this, we plot the frequency vs three different types of scaling of the inner and outer radii which changes the thickness  $T$  of the shell,  $T=R_{out}-R_{in}$ . We choose one mode for this analysis as an illustration—the mode we use is the  $10.4\text{-cm}^{-1}$   $n=1$  mode. We believe this mode is the most intense (in fact only) mode observed in experiment (discussed later). Figure 5(a) shows the effect of changing only the inner radii. In the limit that the inner radii goes to zero, our frequencies and dispersion curves become the same as those reported by Balandin and Fonoberov [14]. Similarly, Fig. 5(b) shows the effect of changing the thickness by varying the outer radius and keeping the inner radius fixed. Finally in Fig. 5(c), we plot the frequency as we uniformly rescale the structure, changing both the inner and outer radii by a scaling factor  $X$ . As can be seen in all three cases, the frequency is (roughly) inversely proportional to the thickness of the shell. This is in line with an approximate  $\omega=ck$  dependence with  $k$  being inversely proportional to the thickness of the tube shell.

With the vibrational frequencies and corresponding Bessel function coefficients determined in the EWT, we can apply Eqs. (26)–(28) to yield the relative Raman intensities of the tubular M13 bacteriophage. The last parameter required for the model is the ratio  $\alpha_c/\alpha_s$ . The parameters  $\alpha_c$  and  $\alpha_s$  [ $\alpha_c = d/9(2\alpha'_{\parallel} + \alpha'_{\perp})$ ,  $\alpha_s = 2d/15(\alpha'_{\parallel} - \alpha'_{\perp}) + 2/5(\alpha_{\parallel} - \alpha_{\perp})$ ] are related to the perpendicular and parallel bond polarizabilities and their derivatives as described in Appendix A. Snoke and Cardona [10] give a comparison between  $\alpha_{\parallel}$  and  $\alpha_{\perp}$  fitted against the Raman spectra for  $C_{60}$  and hydrocarbons for both single and double bonds. For example, in the single bond case of  $C_{60}$ , Snoke and Cardona list fitted parameters of

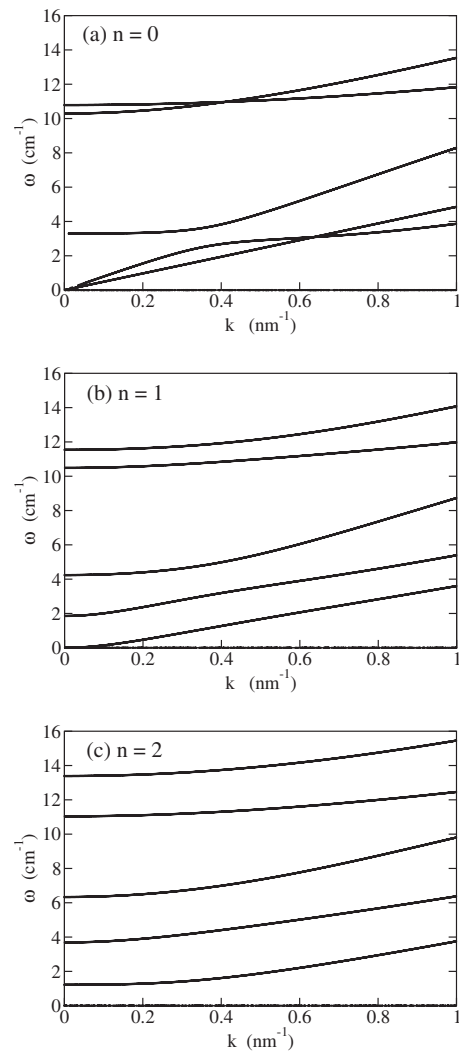


FIG. 4. Frequency dispersion relation  $\omega(k)$  for wave vectors in the EWT model of a cylindrical shell appropriate to M13. The shell has inner and outer radii of 1.9 and 3.4 nm, respectively. (a)  $n=0$ , (b)  $n=1$ , (c)  $n=2$ .

$(\alpha'_{\parallel} - \alpha'_{\perp})/d^2 = 1.2$ ,  $(2\alpha'_{\parallel} + \alpha'_{\perp})/d^2 = 1.7$ , and  $(\alpha_{\parallel} - \alpha_{\perp})/d^3 = 0.5$ , which yields a ratio of  $\alpha_c/\alpha_s = 0.52$ . However, comparison with other fitted parameters shows that  $\alpha_c/\alpha_s$  ranges from 0.26 to 1.0 depending on coordination of the bond and overall structure of the molecule itself. In the case of a long tube composed of various peptides, one expects shearing and compressional forces to result mostly in a stretching of the peptide backbone which is composed mainly of four coordinated carbon atoms with one three coordinated carbon atom. Although there are other atom types such as nitrogen and oxygen in the backbone that can also contribute to the polarizability of the capsid, the AIBP model only requires a single parameter to make qualitative Raman spectra predictions. Thus we choose  $\alpha_c/\alpha_s \approx 0.5$  as a setting for the AIBP model parameter that will reasonably reflect the various types of bonds in the capsid.

The continuum elastic wave model predicts two main types of modes for the cylindrical shell in the long wavelength approximation. They are radial-torsional modes in which  $u_z = 0$ , but  $u_r \neq 0$  and/or  $u_{\theta} \neq 0$ , and axial modes where

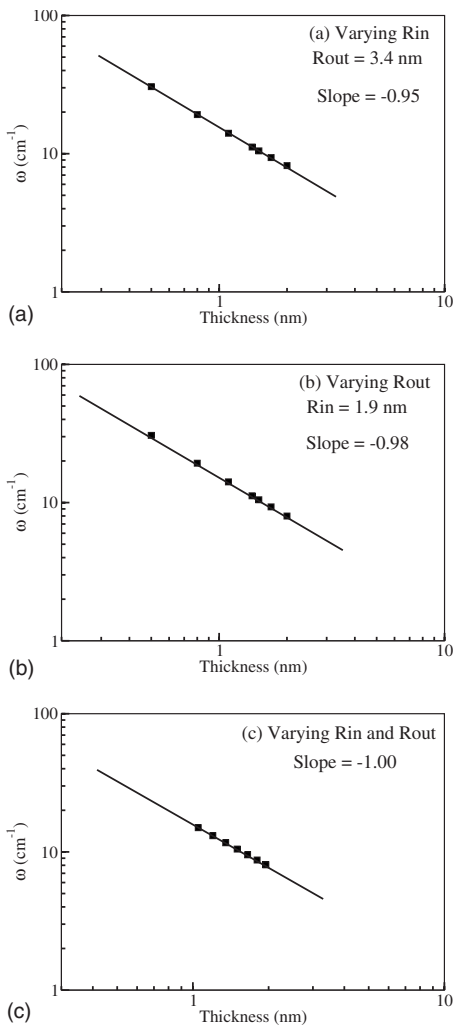


FIG. 5. Log-log plots of the  $10.4\text{-cm}^{-1}$ ,  $n=1$  mode (at  $R_{in} = 1.9$  nm and  $R_{out} = 3.4$  nm) of the cylindrical shell in the EWT model vs thickness  $T$  ( $T = R_{out} - R_{in}$ ). (a) Varying the thickness  $T$  by changing the inner radius  $R_{in}$  only. (b) Varying the thickness  $T$  by changing the outer radius  $R_{out}$  only. (c) Varying the thickness  $T$  by scaling both the inner and outer radii by  $X$  where  $T = X(R_{out} - R_{in})$ .

$u_z \neq 0$ , but  $u_r = u_\theta = 0$ . These two mode types separate at  $k = 0$ , with the  $6 \times 6$  determinant neatly factoring into two smaller determinants; one involving a  $4 \times 4$  matrix that determines the radial and torsional modes, and another  $2 \times 2$  matrix that gives the axial modes. This coupled with the Raman intensity formulas for the cylindrical shell, Eqs. (26)–(28), we find that the Raman active modes of  $n=0$  and  $n=2$  correspond to radial-torsional modes while the  $n=1$  Raman active modes are axial modes.

The total Raman spectra, Figs. 6(a)–6(c), shows that the largest intensity mode is associated with an  $n=1$  axial mode at roughly  $10.4\text{ cm}^{-1}$ . This mode [Fig. 7(a)], whose mode pattern is shown as a cross sectional slice of the  $x$ - $z$  plane of the virus, can be interpreted as an axial shearing mode where the alpha helices forming the capsid are sheared along the fiber axis ( $z$  axis). The next largest Raman peak at approximately  $20.4\text{ cm}^{-1}$  has the pattern shown in in Fig. 7(b) and corresponds to an  $n=0$  radial mode. This mode (shown as a

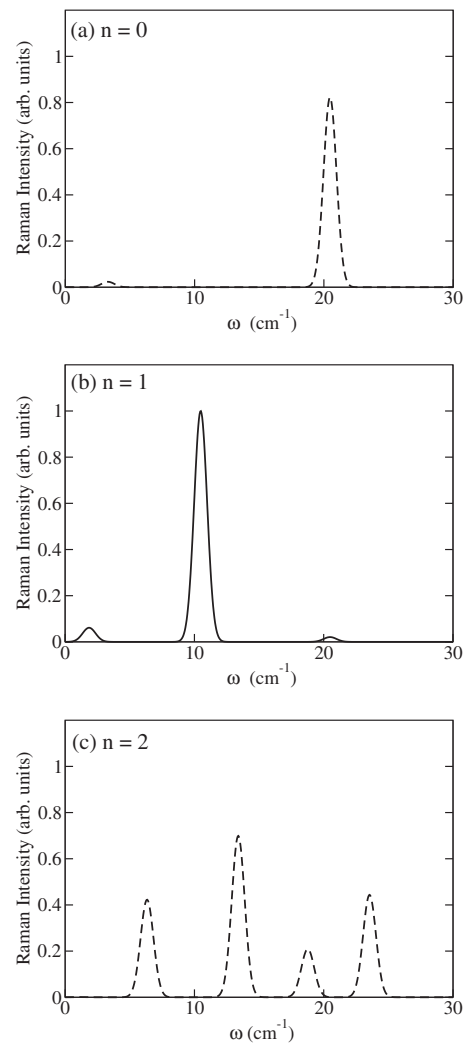


FIG. 6. Theoretical relative Raman intensities of M13 for modes with (a)  $n=0$ , (b)  $n=1$ , (c)  $n=2$ . Dashed lines correspond to radial-torsional modes while solid lines correspond to axial modes. An arbitrary full width at half maximum of  $1\text{ cm}^{-1}$  is used. We hypothesize that the radial-torsional modes (dashed) are highly damped.

cross section through the  $x$ - $y$  plane of the virus) is seen as a radial breathing or compressional mode. The inside radius of the capsid decreases (increases) while the outer radius increases (decreases). All higher frequency modes ( $\omega > 25\text{ cm}^{-1}$ ) have been neglected due to the continuum model losing applicability at higher frequency. As an example, Fig. 7(c) (cross section through the  $x$ - $z$  plane) shows a high frequency  $n=1$  axial mode at roughly  $30.6\text{ cm}^{-1}$ . The displacement pattern for this mode produces waves with wavelength on the order of atomic distances. This is outside the applicability of a continuum model.

It is important to note that no damping effects have been taken into account in the model. One expects some modes to be seriously damped due to the presence of water. We use the displacement patterns themselves to help categorize the modes as likely having high or low damping. For example, we expect the  $n=0$  radial-torsional mode at  $20.4\text{ cm}^{-1}$  to be highly damped when compared with the  $n=1$  axial mode at  $10.4\text{ cm}^{-1}$ . The  $20.4\text{-cm}^{-1}$  radial-torsional mode continually

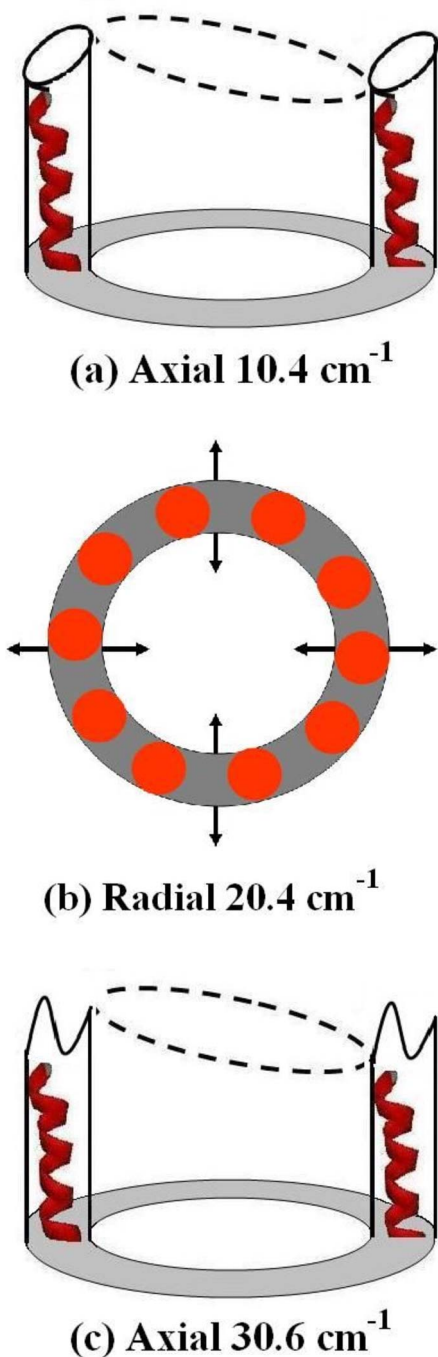


FIG. 7. (Color online) Theoretical displacement patterns for various modes. Axial modes are shown as cross sections through the  $x$ - $z$  plane of the virus while radial modes are shown as cross sections through the  $x$ - $y$  plane of the virus: (a) axial mode at  $10.4 \text{ cm}^{-1}$ , (b) radial-torsional mode at  $20.4 \text{ cm}^{-1}$ , (c) high frequency axial mode at  $30.6 \text{ cm}^{-1}$ .

beats directly against the water on the interior and exterior surfaces of the capsid which produces damping. In contrast, the  $10.4\text{-cm}^{-1}$  axial mode has its displacement along the tube axis, so that at the surface of the capsid, the atoms shear the water rather than beat against it. Thus we expect that axial modes have far less damping. Taking these arguments into account, we hypothesize that in solution there exists signifi-

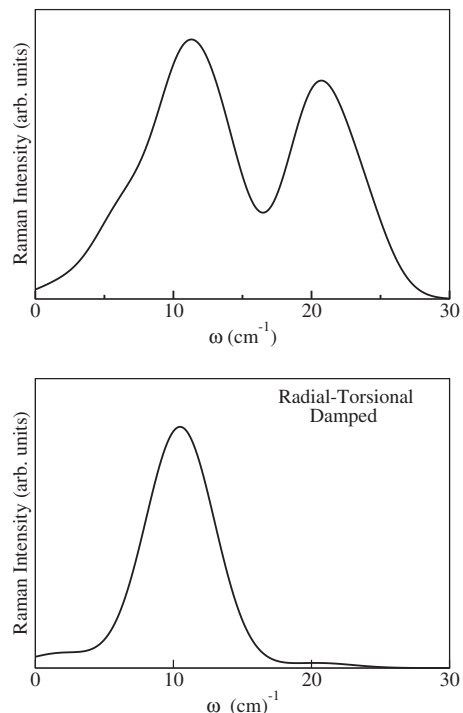


FIG. 8. Theoretical Raman scattering profile of M13 bacteriophage after applying a broadening of  $5 \text{ cm}^{-1}$  to account for the inhomogeneous broadening seen in experiment. Two theoretical profiles are given in order to analyze the possible effects of damping due to the surrounding water. (a) Theoretical Raman profile if no water damping is accounted for, and all modes are included. (b) Theoretical Raman profile if radial-torsional modes are severely damped when compared to the damping of axial modes.

cant damping which dramatically reduces the Raman intensity associated with the radial-torsional modes. Figure 8(a) shows the theoretical Raman intensity profile for the case where *no* damping has been taken into account. The first peak corresponds to the axial mode shown in Fig. 7(a) and the second peak corresponds to the radial mode shown in Fig. 7(b). Figure 8(b) is the theoretical Raman intensity profile where the intensity of radial-torsional modes have been diminished to zero while the intensity of axial modes have been maintained. This qualitatively accounts for damping effects. Figures 8(a) and 8(b) have a broadening of  $5 \text{ cm}^{-1}$  applied to the line shapes to approximate the broadening due to inhomogeneities and other interactions.

We now compare with experimental findings. A full report of the experimental technique and sample preparation has been reported elsewhere [22]. The experimental Raman intensity shown in Fig. 9 gives a single peak at roughly  $8.5 \text{ cm}^{-1}$ . A comparison with the theoretically predicted peaks in Figs. 8(a) (no damping) and 8(b) (damping) shows good agreement with the experimentally observed Raman spectra when our damping hypothesis is taken into account. Accordingly, we assign the observed experimental peak to an excitation of the  $n=1$  axial mode shown in Fig. 7(a).

VI. CONCLUSIONS

This paper uses elastic wave theory along with a bond polarizability model for amorphous materials to determine

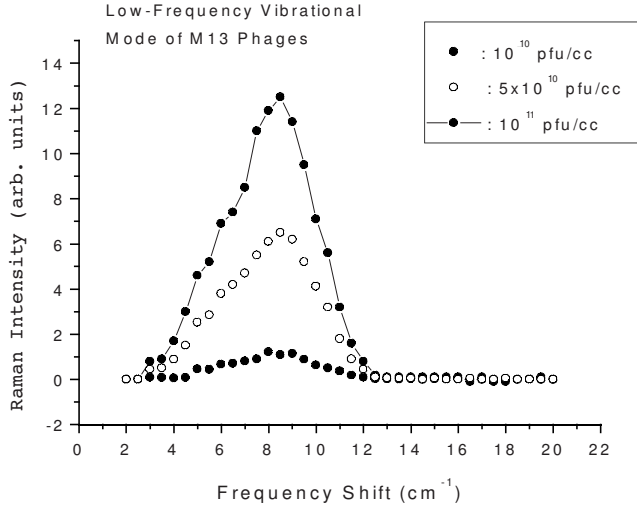


FIG. 9. Experimental Raman intensity of M13 virus obtained from [23]. Three different concentrations of viral particles are shown. The intensity of the peak at  $8.5 \text{ cm}^{-1}$  grows in proportion to viral concentration.

the vibrational frequencies, displacement patterns, and relative Raman intensities for tubular viruses and applies it to the M13 bacteriophage. The developed formulas given by Eqs. (26)–(28) for the Raman intensity and by Eqs. (17)–(19) for the displacement patterns provide a semiquantitative analysis for low frequency vibrational modes of cylindrical viral capsids. When utilized in a comparison with experiment, this theory and the resulting formulas can be used to provide basic predictions concerning the nature of vibrational modes, e.g., axial or radial-torsional, and qualitative estimates of their Raman intensity, as well as the basic displacement pattern associated with the mode.

There are a number of low frequency modes ( $<25 \text{ cm}^{-1}$ ) predicted for the M13 bacteriophage, with six having significant Raman intensity. Of these six modes, only one of them at  $\omega=10.4 \text{ cm}^{-1}$  has axial displacements (along the M13 axis) which produces less damping from the exterior water. The other five modes have a mixture of radial and torsional displacements and thus are expected to experience greater interaction with (hence damping) the water solvent. These findings are compatible with the experimental result that a single peak at  $8.5 \text{ cm}^{-1}$  is observed in the Raman spectra.

The combination of elastic wave theory (EWT) and the amorphous isotropic bond polarizability (AIBP), and generalizations of the Raman intensity formulas of Eqs. (26)–(28) provide a general theoretical framework for qualitative Raman spectra predictions of not only cylindrical viral capsids, but also other shaped viral capsids as well. The methodology can be used generally for disordered materials, as long as a continuum approach is applicable. In the near future, we hope to apply this same type of model to the case of spherical viruses.

#### APPENDIX A: AMORPHOUS ISOTROPIC BOND POLARIZABILITY MODEL

Here we offer a detailed derivation of the amorphous isotropic bond polarizability (AIBP) model. The fundamental

underpinnings are that we model the virus as a collection of two center polarizable bonds, and the bonds are averaged over all orientations as if it were an amorphous isotropic material. We define a bond projection operator for a specific bond by

$$\overleftrightarrow{P} = |\hat{d}\rangle\langle\hat{d}|,$$

where  $\hat{d}$  is the unit direction vector of that bond. This projection operator, when applied to any vector, yields the projection of that vector along the bond axis. The polarizability tensor for a given bond is

$$\overleftrightarrow{\alpha} = \alpha_{\parallel}\overleftrightarrow{P} + \alpha_{\perp}(\overleftrightarrow{I} - \overleftrightarrow{P}), \quad (\text{A1})$$

where  $\alpha_{\parallel}$  and  $\alpha_{\perp}$  are the parallel and perpendicular components of the polarizability. These components depend on the length of the bond distance  $d$ . For small changes of the bond distance due to vibrations, the induced polarizability of the bond is

$$\overleftrightarrow{\Delta\alpha} = \Delta\alpha_{\parallel}\overleftrightarrow{P} + \Delta\alpha_{\perp}(\overleftrightarrow{I} - \overleftrightarrow{P}) + (\alpha_{\parallel} - \alpha_{\perp})\overleftrightarrow{\Delta P}, \quad (\text{A2})$$

where  $\Delta\alpha_{\parallel}$  and  $\Delta\alpha_{\perp}$  describe changes in the parallel and perpendicular polarizability due to a change in bond length

( $\Delta d$ ) while  $\overleftrightarrow{\Delta P}$  describes a change in polarization due to a change in direction of the bond.

The quantities  $\Delta\alpha_{\parallel}$  and  $\Delta\alpha_{\perp}$  can be written in terms of the bond polarizability derivatives to linear order in  $\Delta d$  as

$$\Delta\alpha_{\parallel} = \alpha'_{\parallel}\Delta d, \quad (\text{A3})$$

and

$$\Delta\alpha_{\perp} = \alpha'_{\perp}\Delta d. \quad (\text{A4})$$

Using elasticity theory, we can represent a small change in the bond distance to first order in terms of the strain tensor  $u_{ij}$  by

$$(d + \Delta d)^2 = d^2 \sum_{ij} (\delta_{ij} + 2u_{ij}) \hat{d}_i \hat{d}_j, \quad (\text{A5})$$

or

$$\Delta d \approx d \sum_{ij} u_{ij} \hat{d}_i \hat{d}_j. \quad (\text{A6})$$

Here  $\hat{d}_i$  is the component of  $\hat{d}$  along  $\hat{x}_i$ .

What remains is to write  $\overleftrightarrow{\Delta P}$  from Eq. (A2) in terms of the strain tensor  $u_{ij}$  and then average Eq. (A2) over all bond orientations. The tensor  $\overleftrightarrow{\Delta P}$  is the change of the projector of the bond direction,

$$\overleftrightarrow{\Delta P} = |\hat{d}'\rangle\langle\hat{d}'| - |\hat{d}\rangle\langle\hat{d}|, \quad (\text{A7})$$

where  $\hat{d}'$  denotes the new bond unit direction vector after a small displacement. Noting that to linear order in the strain tensor,

$$|\hat{d}'\rangle = [1 - \langle \hat{d} | \overset{\leftrightarrow}{u} | \hat{d} \rangle \overset{\leftrightarrow}{I}] |\hat{d}\rangle + \overset{\leftrightarrow}{u} |\hat{d}\rangle, \quad (\text{A8})$$

and that the strain tensor is symmetric and real, Eq. (A7) can be written as

$$\overset{\leftrightarrow}{\Delta P} = |\hat{d}\rangle \langle \hat{d}| \overset{\leftrightarrow}{u} + \overset{\leftrightarrow}{u} |\hat{d}\rangle \langle \hat{d}| - 2 \langle \hat{d} | \overset{\leftrightarrow}{u} | \hat{d} \rangle |\hat{d}\rangle \langle \hat{d}|. \quad (\text{A9})$$

We now have all the pieces to compute the average of Eq. (A2). Utilizing Eqs. (A3) and (A4) in Eq. (A2) and averaging over the solid angle gives

$$\langle \overset{\leftrightarrow}{\Delta \alpha} \rangle_{\Omega} = (\alpha'_{\parallel} - \alpha'_{\perp}) \langle \overset{\leftrightarrow}{P \Delta d} \rangle_{\Omega} + \alpha'_{\perp} \overset{\leftrightarrow}{I} \langle \overset{\leftrightarrow}{\Delta d} \rangle_{\Omega} + (\alpha_{\parallel} - \alpha_{\perp}) \langle \overset{\leftrightarrow}{\Delta P} \rangle_{\Omega}. \quad (\text{A10})$$

The components of the direction vector in spherical polar angles are  $\hat{d}_x = \cos \phi \sin \theta$ ,  $\hat{d}_y = \sin \phi \sin \theta$ , and  $\hat{d}_z = \cos \theta$ . Using the following averages over bond directions:

$$\langle \hat{d}_i \hat{d}_j \rangle_{\Omega} = \frac{1}{3} \delta_{ij},$$

$$\langle \hat{d}_i^2 \hat{d}_j^2 \rangle_{\Omega} = \frac{1}{5} \delta_{ij} + \frac{1}{15} (1 - \delta_{ij}), \quad (\text{A11})$$

a component of the induced polarizability in Eq. (A10) can be written as

$$\begin{aligned} \langle \overset{\leftrightarrow}{\Delta \alpha_{ij}} \rangle_{\Omega} &= \frac{2}{15} d(\alpha'_{\parallel} - \alpha'_{\perp}) \left( u_{ij} + \frac{1}{2} \text{Tr}(\overset{\leftrightarrow}{u}) \delta_{ij} \right) + \frac{2}{5} (\alpha_{\parallel} - \alpha_{\perp}) \\ &\times \left( u_{ij} - \frac{1}{3} \text{Tr}(\overset{\leftrightarrow}{u}) \delta_{ij} \right) + \frac{1}{3} d \alpha'_{\perp} \text{Tr}(\overset{\leftrightarrow}{u}) \delta_{ij}. \end{aligned} \quad (\text{A12})$$

Making the following definitions for the shear ( $s$ ) and compressional ( $c$ ) components:

$$\begin{aligned} \alpha_s &\equiv \frac{2}{5} \left( \frac{d(\alpha'_{\parallel} - \alpha'_{\perp})}{3} + (\alpha_{\parallel} - \alpha_{\perp}) \right), \\ \alpha_c &\equiv \frac{d}{9} (\alpha'_{\parallel} + 2\alpha'_{\perp}), \end{aligned} \quad (\text{A13})$$

and using the shear strain tensor,

$$\overset{\leftrightarrow}{u}_s = \overset{\leftrightarrow}{u} - \frac{1}{3} \text{Tr}(\overset{\leftrightarrow}{u}) \overset{\leftrightarrow}{I},$$

we obtain the final result for the induced polarizability of a single bond in the AIBP model,

$$\overset{\leftrightarrow}{\Delta \alpha} = \alpha_s \overset{\leftrightarrow}{u}_s + \alpha_c \text{Tr}(\overset{\leftrightarrow}{u}) \overset{\leftrightarrow}{I}. \quad (\text{A14})$$

Assuming that each bond occupies an average volume of  $V_b$ , the induced polarizability per unit volume is

$$\overset{\leftrightarrow}{\Delta \alpha} = \frac{\alpha_s}{V_b} \overset{\leftrightarrow}{u}_s + \frac{\alpha_c}{V_b} \text{Tr}(\overset{\leftrightarrow}{u}) \overset{\leftrightarrow}{I}. \quad (\text{A15})$$

This formula then determines the change in polarizability do to a strain. Given the displacement patterns of the modes

[Eqs. (17)–(19)], the strain tensors  $\overset{\leftrightarrow}{u}_s$  and  $\overset{\leftrightarrow}{u}$  may be computed to give the change in polarization.

## APPENDIX B: RAMAN INTENSITY FORMULA

In this section, we discuss the factors necessary to produce estimates for the Raman intensity using the AIBP model. We begin by considering two frames of reference for the cylindrical virus: (i) the frame of reference with respect to the laboratory (unprimed,  $\hat{x}\hat{y}\hat{z}$ ), where light is emitted and received, and (ii) the frame of reference of the fiber (primed,  $\hat{x}'\hat{y}'\hat{z}'$ ), where the cylindrical shell is orientated along the  $\hat{z}'$  axis. These two frames are connected via a simple rotation matrix

$$\overset{\leftrightarrow}{R}(\theta, \phi, \psi) \quad \text{with} \quad \begin{cases} 0 \leq \theta \leq \pi \\ 0 \leq \phi \leq 2\pi, \\ 0 \leq \psi \leq 2\pi \end{cases} \quad (\text{B1})$$

where  $\theta$ ,  $\phi$ , and  $\psi$  can be chosen to be the Euler angles [24]. The transformation of a general vector  $\mathbf{v}$  between the laboratory and the fiber frames is then given by

$$\overset{\leftrightarrow}{\mathbf{v}'} = \overset{\leftrightarrow}{R} \overset{\leftrightarrow}{\mathbf{v}} \quad (\text{or}) \quad \overset{\leftrightarrow}{\mathbf{v}} = \overset{\leftrightarrow}{R}^{\dagger} \overset{\leftrightarrow}{\mathbf{v}'}.$$

The laboratory axes (as viewed in the fiber frame) can be obtained by an application of the rotation matrix to the laboratory axes

$$\begin{aligned} \overset{\leftrightarrow}{R}\hat{x} &= (\cos \phi \cos \psi - \cos \theta \sin \phi \sin \psi) \hat{x}' \\ &+ (\sin \phi \cos \psi + \cos \theta \cos \phi \sin \psi) \hat{y}' + (\sin \theta \sin \psi) \hat{z}', \\ \overset{\leftrightarrow}{R}\hat{y} &= (-\cos \phi \sin \psi - \cos \theta \sin \phi \cos \psi) \hat{x}' \\ &+ (-\sin \phi \sin \psi + \cos \theta \cos \phi \cos \psi) \hat{y}' \\ &+ (\sin \theta \cos \psi) \hat{z}', \\ \overset{\leftrightarrow}{R}\hat{z} &= \sin \theta \sin \phi \hat{x}' - \sin \theta \cos \phi \hat{y}' + \cos \theta \hat{z}'. \end{aligned}$$

We will adopt the following notation of the above expressions, which will help when performing averages later:

$$\overset{\leftrightarrow}{R}\hat{x} = x_1 \hat{x}' + x_2 \hat{y}' + x_3 \hat{z}', \quad (\text{B2})$$

$$\overset{\leftrightarrow}{R}\hat{y} = y_1 \hat{x}' + y_2 \hat{y}' + y_3 \hat{z}', \quad (\text{B3})$$

$$\overset{\leftrightarrow}{R}\hat{z} = z_1 \hat{x}' + z_2 \hat{y}' + z_3 \hat{z}'. \quad (\text{B4})$$

The coefficients  $x_i$ ,  $y_i$ , and  $z_i$  can be identified as simply the column elements of the Euler rotation matrix.

The rotation matrix is capable of describing any orientation of the cylindrical shell with respect to the lab frame. It is desirable to work out the Raman intensity in the fiber frame of reference. In this frame the fiber always has the same orientation and thus the same susceptibility tensor. Our

analysis in this section thus focuses on the fiber frame.

To evaluate the Raman intensities of vibrational modes of a cylindrical viral capsid, we imagine the scattering processes involved. In a general Raman spectroscopy experiment, light is emitted from a source (propagating along the lab  $z$  axis) with frequency  $\omega_L$ . The light source transfers energy in the form of a phonon to the virus capsid. This causes the virus capsid to vibrate (Stokes shift) at a frequency  $\omega$  that is determined from harmonic analysis. The susceptibility of the viral particle also varies temporally at this frequency. The resultant fluctuations in the total polarization of the particle causes the scattered light to shift frequencies to  $\omega_L - \omega$  which is received by the detector. The intensity of the scattered light received by a detector is proportional to

$$I \propto \frac{1}{\omega} \left| \overset{\leftrightarrow}{e}'_s \overset{\leftrightarrow}{\Delta\chi} \overset{\leftrightarrow}{e}'_i \right|^2, \quad (\text{B5})$$

where  $\overset{\leftrightarrow}{e}'_s$  and  $\overset{\leftrightarrow}{e}'_i$  are the polarization directions of the scattered and incident light as viewed in the fiber frame. The susceptibility tensor  $\overset{\leftrightarrow}{\Delta\chi}$  describes the *change* in the susceptibility of the virus due to the vibrational mode ( $\overset{\leftrightarrow}{\Delta\chi} = \int \overset{\leftrightarrow}{\Delta\alpha} dV$ ). Appendix A describes the calculation of this tensor; here the Raman intensity is evaluated in terms of a general susceptibility tensor. There are two possible polarizations for the scattered light corresponding to the directions in the plane perpendicular to the direction of propagation. The total scattered intensity is given by

$$I \propto \frac{1}{\omega} \left| \overset{\leftrightarrow}{e}'_{s1} \overset{\leftrightarrow}{\Delta\chi} \overset{\leftrightarrow}{e}'_i \right|^2 + \frac{1}{\omega} \left| \overset{\leftrightarrow}{e}'_{s2} \overset{\leftrightarrow}{\Delta\chi} \overset{\leftrightarrow}{e}'_i \right|^2. \quad (\text{B6})$$

Since the viral particles in solution have random orientations with respect to the incident light, the above equation must then be averaged over all orientations of the fiber frame, relative to the lab frame.

The incident light propagates along  $z$ , and the polarization can be written in terms of  $x$  and  $y$  components in the Laboratory frame as

$$\overset{\leftrightarrow}{e}_i = \cos \theta_i \overset{\leftrightarrow}{x} + \sin \theta_i \overset{\leftrightarrow}{y}. \quad (\text{B7})$$

The propagation direction of the scattered light will be treated in general; i.e., the scattered light propagates along a direction given by the spherical polar angles  $\Phi$  and  $\Theta$  (see Fig. 1). Polarization of the light can be in either of two mutually orthogonal directions perpendicular to the propagation direction. In the laboratory frame these are

$$\overset{\leftrightarrow}{e}'_{s1} = \cos \Phi \cos \Theta \overset{\leftrightarrow}{x} + \sin \Phi \cos \Theta \overset{\leftrightarrow}{y} - \sin \Theta \overset{\leftrightarrow}{z}, \quad (\text{B8})$$

$$\overset{\leftrightarrow}{e}'_{s2} = -\sin \Phi \overset{\leftrightarrow}{x} + \cos \Phi \overset{\leftrightarrow}{y}. \quad (\text{B9})$$

We now transform the polarization vectors from the laboratory frame  $(\overset{\leftrightarrow}{x}, \overset{\leftrightarrow}{y}, \overset{\leftrightarrow}{z})$  to the fiber frame  $(\overset{\leftrightarrow}{x}', \overset{\leftrightarrow}{y}', \overset{\leftrightarrow}{z}')$  by applying the Euler rotation matrix:

$$\begin{aligned} \overset{\leftrightarrow}{e}'_i &= \overset{\leftrightarrow}{R} \overset{\leftrightarrow}{e}_i = \cos \theta_i \overset{\leftrightarrow}{R} \overset{\leftrightarrow}{x} + \sin \theta_i \overset{\leftrightarrow}{R} \overset{\leftrightarrow}{y}, \\ \overset{\leftrightarrow}{e}'_{s1} &= \cos \Phi \cos \Theta \overset{\leftrightarrow}{R} \overset{\leftrightarrow}{x} + \sin \Phi \cos \Theta \overset{\leftrightarrow}{R} \overset{\leftrightarrow}{y} - \sin \Theta \overset{\leftrightarrow}{R} \overset{\leftrightarrow}{z}, \\ \overset{\leftrightarrow}{e}'_{s2} &= -\sin \Phi \overset{\leftrightarrow}{R} \overset{\leftrightarrow}{x} + \cos \Phi \overset{\leftrightarrow}{R} \overset{\leftrightarrow}{y}. \end{aligned}$$

These equations can then be written in terms of the coefficients  $x_i$ ,  $y_i$ , and  $z_i$  [Eqs. (B2)–(B4)].

We now turn our attention toward the averaging process. With the above polarization directions and a general susceptibility tensor  $\overset{\leftrightarrow}{\Delta\chi}$ , all that remains is to calculate the average intensity,

$$I_{avg} = \langle I \rangle = \int P(\phi, \theta, \psi, \theta_i) Id\Omega,$$

where  $\phi$ ,  $\theta$ , and  $\psi$  are the Euler angles that give the orientation of the cylindrical virus with respect to the laboratory frame, and  $\theta_i$  is the angle that describes the polarization of the incident light. Here, we treat the case of unpolarized incident light. In this case, since all angles are assumed equally likely, our probability must be given by a constant:

$$P(\phi, \theta, \psi, \theta_i) = \frac{1}{16\pi^3},$$

with

$$d\Omega = \sin \theta d\theta d\phi d\psi d\theta_i.$$

Using Eq. (B7) and Eqs. (B8) and (B9) in the intensity formula, Eq. (B6), we obtain terms in the intensity proportional to one of the three following forms:

$$\cos^2 \theta_i a_i b_m x_j x_n \overset{\leftrightarrow}{\Delta\chi}_{ij} \overset{\leftrightarrow}{\Delta\chi}_{mn},$$

$$\cos \theta_i \sin \theta_i a_i b_m x_j y_n \overset{\leftrightarrow}{\Delta\chi}_{ij} \overset{\leftrightarrow}{\Delta\chi}_{mn},$$

$$\sin^2 \theta_i a_i b_m y_j y_n \overset{\leftrightarrow}{\Delta\chi}_{ij} \overset{\leftrightarrow}{\Delta\chi}_{mn},$$

where  $a_i$  and  $b_i$  denote any of the coefficients  $x_i$ ,  $y_i$ , or  $z_i$ . The second of the three terms vanishes when integrated over  $\theta_i$  in the average intensity. In addition, the only surviving averages  $\langle a_i b_m x_j x_n \rangle$  and  $\langle a_i b_m y_j y_n \rangle$  are

$$\langle a_i a_i a_i a_i \rangle = \frac{1}{5},$$

$$\langle a_i a_i a_j a_j \rangle = \frac{1}{15},$$

$$\langle a_i a_i b_j b_j \rangle = \frac{1}{15},$$

$$\langle a_i a_i b_j b_j \rangle = \frac{2}{15},$$

$$\langle a_i a_j b_i b_j \rangle = -\frac{1}{30}. \quad (\text{B10})$$

Thus we can write the average intensity as

$$\begin{aligned} \omega I_{avg} &\propto (\cos^2\Theta \cos^2\Phi + \sin^2\Phi) \\ &\times \sum_{ijmn} \Delta\chi_{ij}\Delta\chi_{mn} [\langle x_i x_m x_j x_n \rangle + \langle x_i x_m y_j y_n \rangle] \\ &+ (\cos^2\Theta \sin^2\Phi + \cos^2\Phi) \sum_{ijmn} \Delta\chi_{ij}\Delta\chi_{mn} [\langle y_i y_m x_j x_n \rangle \\ &+ \langle y_i y_m y_j y_n \rangle] + \sin^2\Theta \sum_{ijmn} \Delta\chi_{ij}\Delta\chi_{mn} [\langle z_i z_m x_j x_n \rangle \\ &+ \langle z_i z_m y_j y_n \rangle]. \end{aligned} \quad (\text{B11})$$

Utilizing Eq. (B10) and the case of a symmetric susceptibility tensor, Eq. (B11) takes the form

$$\begin{aligned} \omega I_{avg} &\propto [16 - 4 \sin^2\Theta] (|\Delta\chi_{xx}|^2 + |\Delta\chi_{yy}|^2 + |\Delta\chi_{zz}|^2) \\ &+ [4 - 6 \sin^2\Theta] (\Delta\chi_{xx}\Delta\chi_{yy} + \Delta\chi_{xx}\Delta\chi_{zz} + \Delta\chi_{yy}\Delta\chi_{zz}) \\ &+ [14 - \sin^2\Theta] (|\Delta\chi_{xy}|^2 + |\Delta\chi_{xz}|^2 + |\Delta\chi_{yz}|^2). \end{aligned} \quad (\text{B12})$$

Finally, we can combine this into a form similar to the elastic free energy of a material with constants  $\lambda_R$  and  $\mu_R$ :

$$I_{avg} \propto \frac{1}{2} \frac{\lambda_R}{\omega} [\text{Tr}(\overleftrightarrow{\Delta\chi})]^2 + \frac{\mu_R}{\omega} \text{Tr}([\overleftrightarrow{\Delta\chi}]^2) \quad (\text{B13})$$

The constants  $\lambda_R$  and  $\mu_R$  describe the orientation of the detector and are given by

$$\lambda_R \equiv [4 - 6 \sin^2\Theta], \quad (\text{B14})$$

$$\mu_R \equiv [14 - \sin^2\Theta]. \quad (\text{B15})$$

- 
- [1] W. Shenton, T. Douglas, M. Young, G. Stubbs, and S. Mann, *Adv. Mater. (Weinheim, Ger.)* **11**, 253 (1999).
- [2] M. Knez, M. Sumser, A. M. Bittner, C. Wege, H. Jeske, T. P. Martin, and K. Kern, *Adv. Funct. Mater.* **14**, 116 (2004).
- [3] C. Mao, D. J. Solis, B. D. Reiss, S. T. Kottmann, R. Y. Sweeney, A. Hayhurst, G. Georgiou, B. Iverson, and A. M. Belcher, *Science* **303**, 213 (2004).
- [4] P. L. Freddolino, A. S. Arkipov, S. B. Larson, A. McPherson, and K. Schulten, *Structure (London)* **14**, 437 (2006).
- [5] F. Tama and C. L. Brooks III, *J. Mol. Biol.* **345**, 299 (2005).
- [6] F. Tama and C. L. Brooks III, *Annu. Rev. Biophys. Biomol. Struct.* **35**, 115 (2006).
- [7] H. Lamb, *Proc. London Math. Soc.* **13**, 187 (1882).
- [8] L. H. Ford, *Phys. Rev. E* **67**, 051924 (2003).
- [9] S. Go, H. Bilz, and M. Cardona, *Phys. Rev. Lett.* **34**, 580 (1975).
- [10] D. W. Snoke and M. Cardona, *Solid State Commun.* **87**, 121 (1993).
- [11] D. B. Murray, C. H. Netting, R. Mercer, and L. Saviot, e-print arXiv:cond-mat/0608102.
- [12] K. F. Graff, *Wave Motion in Elastic Solids* (Ohio State University Press, New York, 1991).
- [13] L. D. Landau and E. M. Lifshitz, *Theory of Elasticity*, (Pergamon, New York, 2001).
- [14] A. A. Balandin and V. A. Fonoberov, *Journal of Biomedical Nanotechnology* **1**, 90 (2005).
- [15] N. W. Ashcroft and N. D. Mermin, *Solid State Physics* (Saunders College, Philadelphia, 1976), p. 481.
- [16] J. Dong and O. F. Sankey, *J. Appl. Phys.* **87**, 7726 (2000).
- [17] S. Guha, J. Menendez, J. B. Page, and G. B. Adams, *Phys. Rev. B* **53**, 13106 (1996).
- [18] D. A. Marvin, L. C. Welsh, M. F. Symmons, W. R. P. Scott, and S. K. Strauss, *J. Mol. Biol.* **355**, 294 (2006).
- [19] M. Tachibana, K. Kojima, R. Ikuyama, Y. Kobayashi, and M. Ataka, *Chem. Phys. Lett.* **332**, 259 (2000).
- [20] V. A. Fonoberov and A. A. Balandin, *Phys. Status Solidi B* **241**, R67 (2004).
- [21] M. Talati and P. K. Jha, *Phys. Rev. E* **73**, 011901 (2006).
- [22] K. T. Tsen, E. Dykeman, O. F. Sankey, N.-T. Lin, S.-W. D. Tsen, and J. G. Kiang, *J. Virol.* **3**, 79 (2006).
- [23] K. T. Tsen, E. C. Dykeman, O. F. Sankey, S.-W. D. Tsen, N.-T. Lin, and J. G. Kiang, *Nanotechnology* **17**, 5474 (2006).
- [24] H. Goldstein, *Classical Mechanics* (Addison-Wesley, Reading, MA, 1965), p. 107.